

# High resolution strain mapping of a single axially heterostructured nanowire using scanning X-ray diffraction

Susanna Hammarberg<sup>1</sup> (✉), Vilgailė Dagitė<sup>2</sup>, Lert Chayanun<sup>1</sup>, Megan O. Hill<sup>3</sup>, Alexander Wyke<sup>1</sup>, Alexander Björling<sup>4</sup>, Ulf Johansson<sup>4</sup>, Sebastian Kalbfleisch<sup>4</sup>, Magnus Heurlin<sup>2</sup>, Lincoln J. Lauhon<sup>3</sup>, Magnus T. Borgström<sup>2</sup>, and Jesper Wallentin<sup>1</sup>

<sup>1</sup> Synchrotron Radiation Research and NanoLund, Lund University, Box 118, Lund 221 00, Sweden

<sup>2</sup> Solid State Physics and NanoLund, Lund University, Box 118, Lund 221 00, Sweden

<sup>3</sup> Department of Materials Science and Engineering, Northwestern University, Evanston, Illinois 60208, USA

<sup>4</sup> MAX IV Laboratory, Lund University, Box 118, Lund 221 00, Sweden

© The author(s) 2020

Received: 27 March 2020 / Revised: 12 May 2020 / Accepted: 13 May 2020

## ABSTRACT

Axially heterostructured nanowires are a promising platform for next generation electronic and optoelectronic devices. Reports based on theoretical modeling have predicted more complex strain distributions and increased critical layer thicknesses than in thin films, due to lateral strain relaxation at the surface, but the understanding of the growth and strain distributions in these complex structures is hampered by the lack of high-resolution characterization techniques. Here, we demonstrate strain mapping of an axially segmented GaInP-InP 190 nm diameter nanowire heterostructure using scanning X-ray diffraction. We systematically investigate the strain distribution and lattice tilt in three different segment lengths from 45 to 170 nm, obtaining strain maps with about  $10^{-4}$  relative strain sensitivity. The experiments were performed using the 90 nm diameter nanofocus at the NanoMAX beamline, taking advantage of the high coherent flux from the first diffraction limited storage ring MAX IV. The experimental results are in good agreement with a full simulation of the experiment based on a three-dimensional (3D) finite element model. The largest segments show a complex profile, where the lateral strain relaxation at the surface leads to a dome-shaped strain distribution from the mismatched interfaces, and a change from tensile to compressive strain within a single segment. The lattice tilt maps show a cross-shaped profile with excellent qualitative and quantitative agreement with the simulations. In contrast, the shortest measured InP segment is almost fully adapted to the surrounding GaInP segments.

## KEYWORDS

strain mapping, nanowire, heterostructure, X-ray diffraction (XRD), MAX IV, finite element modeling

## 1 Introduction

Semiconductor heterostructures are crucial building blocks for most modern electronic and optoelectronic devices. As such, extensive research has been devoted to creating tailorable, pristine interfaces between semiconductor thin films. However, this has been limited to low lattice mismatch materials, as large interfacial strain can lead to defect formation and device degradation. Nanowire heterostructures on the other hand have allowed for the creation of new heterostructures, given their high strain tolerance. Nanowires are a class of one-dimensional semiconductor nanostructures that are being developed for electronics [1–3], photovoltaics [4–6], detectors [7], and light emitting devices [8–11], as well as studies of quantum physics [12–16]. In addition to new flexibility in heterostructure material combinations compared with bulk material, the small dimensions of nanowires also result in reduced material usage and high scalability. Nanowire synthesis also has more degrees of freedom than traditional thin film growth, allowing controlled heterostructure formation both axially [17] and radially [18]. Heterostructures in the axial direction are particularly interesting

because they can modify the band structure along the natural carrier transport direction, and such nanowires are being explored both for fundamental physics [19] as well as for devices such as multijunction solar cells [20, 21], tunnel diodes [22], tunneling field effect transistors [1], and lasers [23].

Given the presence of lattice mismatched interfaces, it is critical to understand the strain state at nanowire junctions, because the strain can affect the bandgap and the charge carrier mobility as well as induce piezoelectric fields. Furthermore, while the growth of lattice mismatched heterostructures is quite well understood in epitaxial films, nanowire heterostructures are more complex. In thin films, defects form when the layer exceeds a critical thickness, which is generally problematic since they form carrier recombination and scattering centers. Theoretical studies have predicted that the strain at the interface of an axially heterostructured nanowire could be partially accommodated by lateral expansion or compression via the free surfaces [24–26], which means that segments with larger lattice mismatch than predicted for thin films could be grown without defect formation. Simulations based on finite element modelling (FEM) have predicted dome-shaped strain

Address correspondence to [susanna.hammarberg@sljus.lu.se](mailto:susanna.hammarberg@sljus.lu.se)

distributions at the interface, with maximum strain at the radial centre of the nanowire [25, 27]. This three-dimensional (3D) strain relaxation becomes comparatively more important in thinner nanowires, and for a given misfit, theoretical calculations predict a critical radius below which infinitely thick layers can be grown defect free [24–26]. However, the theoretical models typically ignore experimentally observed complexities such as nanowire bending [28], phase segregation [29] and interdiffusion [30]. Therefore, quantitative high-resolution strain measurements, combined with theoretical calculations, are vital for fully understanding axial nanowire heterostructures.

Experimental characterization of the strain distribution in axial nanowire heterostructures is challenging, due to the simultaneous requirements of high strain sensitivity and spatial resolution. Transmission electron microscopy (TEM) offers excellent spatial resolution but limited strain sensitivity, and it has therefore been used for studies of axial heterostructures with quite large mismatches [30, 31]. The strong interaction of electron probes with matter also limits TEM to studies of relatively thin nanowires. In comparison, the strain sensitivity of X-ray diffraction (XRD) is excellent, typically significantly better than TEM, and the long absorption length of hard X-rays allows studies of large crystals in a non-destructive manner. Traditionally, XRD has had limited real space resolution due to the difficulty in making high-quality X-ray optics, but development in focusing techniques has given the opportunity to focus a highly coherent hard X-ray beam down to the nanoscale [32, 33]. These improvements have enabled diffraction imaging of single nanocrystal structures to study the strain distribution [34–37], detect defects and dislocations [38], as well as complete devices [39] under applied voltage [40, 41]. Strain mapping of axially heterostructured nanowires with high spatial resolution and strain sensitivity has so far not been demonstrated, to the best of our knowledge, partially because such weakly scattering nanocrystals require an intense X-ray nanofocus. However, a new generation of so-called diffraction

limited storage rings (DLSR) have been developed, which offer much higher coherent X-ray fluxes [42] than previous synchrotrons.

Here, we demonstrate high-resolution strain mapping of an axially heterostructured  $\text{Ga}_x\text{In}_{1-x}\text{P-InP}$  nanowire using the NanoMAX beamline [43] of the MAX IV facility, the first operational DLSR.  $\text{Ga}_x\text{In}_{1-x}\text{P}$  (hereafter referred to as GaInP) is a promising material for photovoltaics and light emitting devices, as its bandgap can be adjusted from the near-infrared region to the middle of the visible spectra by changing the relative amount of Ga and In. We use scanning XRD with a 90 nm beam to obtain two-dimensional (2D) maps of the strain, with about  $10^{-4}$  relative strain sensitivity, as well as the lattice tilt. We probe the strain distribution at different axial layer thicknesses within a single nanowire and find that the segment length strongly affects both the average strain and the strain distribution. The 3D strain profile of the nanowire heterostructure was simulated using FEM and the experimental data was compared with kinematic scattering simulations based on the FEM result and the measured beam profile. The measurements of the GaInP segments and the longest InP segment verify the theoretically predicted strain distributions, where both materials show similar but mirrored dome-shaped strain profiles with both positive and negative strains within the same segment. In contrast, the shortest investigated InP segment is almost fully homogeneous and adapted to the surrounding GaInP lattice. Our results demonstrate that nanofocused XRD has sufficient strain sensitivity and spatial resolution to measure the strain distribution in axially heterostructured nanowires.

## 2 Experimental

Nanowires consisting of five InP segments of varied length within a GaInP nanowire were grown in the particle assisted growth mode using metal-organic vapor phase epitaxy (Figs. 1(a) and 1(b)). The Au seed particle array was defined

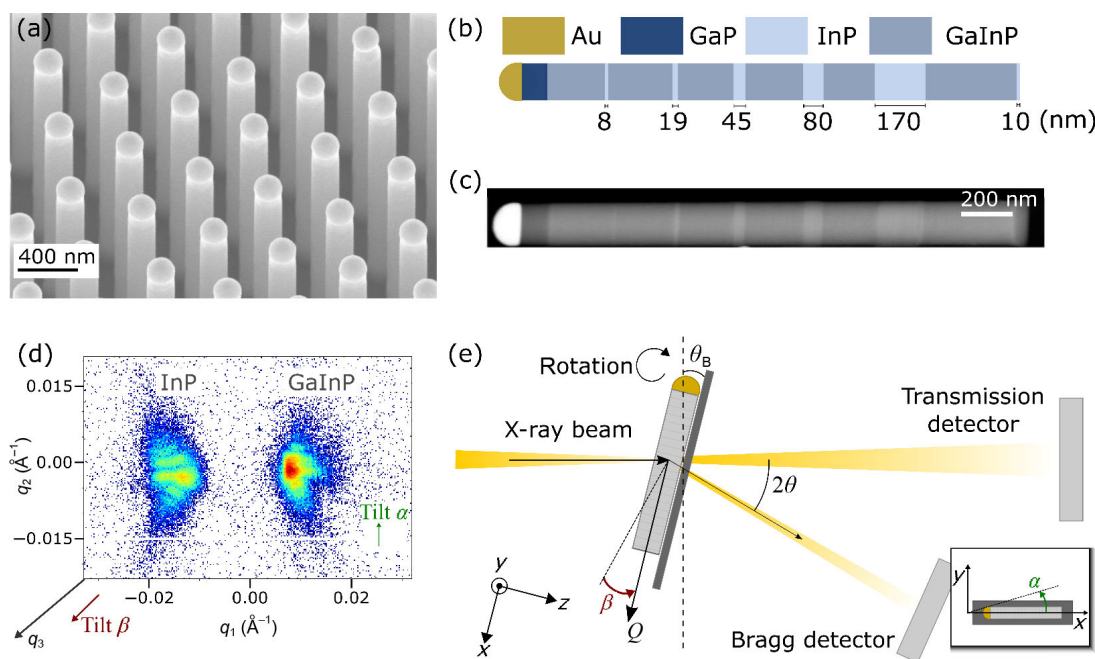


**Figure 1** Experimental setup. (a) Scanning electron microscopy (SEM) image of an array of GaInP-InP nanowire heterostructures as grown on the substrate from Au seed particles. The image was taken at a tilt of  $30^\circ$ . (b) Sketch of a single nanowire with approximate InP segment lengths. (c) STEM image of a single nanowire. (d) Example of Bragg diffraction signal from the (111) lattice planes of a single nanowire in the experiment. The signal is the logarithm of the sum of all frames over a rocking curve in a single position on the wire, with the InP peak to the left and the GaInP peak to the right. The detector frames' reciprocal space vectors ( $q_1, q_2, q_3$ ) directions are indicated. (e) Experimental geometry as viewed from above. The nanowire is lying flat on a  $\text{Si}_3\text{N}_4$  window. The tilt  $\beta$  is around the same axis as  $\theta$ . The inset indicates the tilt  $\alpha$ , which is a rotation around  $z$ .

by nanoimprint lithography, resulting in a hexagonal pattern of Au particles with a pitch of 500 nm [44]. The nanowires show an average radius of about 95 nm, which is slightly above the predicted critical radius for the lattice mismatch [25, 26]. The total length was about 2.2  $\mu\text{m}$  for nanowires from the center of the growth substrate, whereas the nanowire growth rate was higher towards the edges of the substrate. High angle annular dark field scanning transmission electron microscopy (HAADF-STEM) of a single nanowire is shown in Fig. 1(c), where the denser InP segments are brighter, exhibiting a barcode structure. The lengths of each segment, obtained from STEM measurements, were 170, 80, 45, 19, and 8 nm corresponding to segment growth times of 120, 60, 45, 30, and 15 s, respectively. The nanowires grow in the (111)B direction and have a zinc blende crystal structure.

To prepare for nano-XRD, nanowires were mechanically transferred to a  $\text{Si}_3\text{N}_4$  membrane, lying flat on the surface in random in-plane orientations. We used the Kirkpatrick-Baez (KB) mirror nanofocus at NanoMAX to perform scanning XRD of a single heterostructured nanowire (energy 9.49 keV, flux  $10^9$  photons/s, focus size 90 nm). The beamline's secondary source aperture slits were adjusted to ensure a coherent illumination incident on the KB-mirrors [45].

We used one 2D detector in transmission to track the real space movement of the sample and for ptychographic probe reconstructions, and a second one for the Bragg diffraction. We collected scanning XRD data sets from the (111) reflection, i.e. with the scattering vector parallel to the nanowire axis, by 2D scanning the sample in focus. A rocking curve was collected by rotating the sample around  $\gamma$  in 51 angular steps of  $0.02^\circ$  (see the coordinate system and the scattering geometry as viewed from above in Fig. 1(e)). Between rotations, we tracked and compensated for systematic and unsystematic movements of the nanowire by analyzing the transmission signal, as discussed in the Methods section. We used a fly scanning mode in the horizontal direction to minimize the overhead, by moving the piezo scanner continuously while acquiring 101 frames in a 3  $\mu\text{m}$  range. In the vertical direction, we used a 40 nm step size. The high coherent flux allowed a short acquisition time of 0.12 s per frame, giving a total measurement time of 4 h for the dataset consisting of 96,960 frames. Due to the modest lattice mismatch, we could collect the two peaks of InP and GaInP on the detector simultaneously, see an example of the scattered signal in Fig. 1(d). The complex shape of the Bragg peaks comes from the finite size of the segments and the beam, as well as strain, as discussed further in Section 3.3. For each beam position, we made reciprocal space mapping [46] of the InP and GaInP Bragg peaks and calculated the respective peak positions using the center of mass.

### 3 Results and discussion

#### 3.1 Strain maps of a nanowire heterostructure

The results from the analysis of the scanning XRD measurements are shown in Fig. 2(a), with the InP to the left and GaInP to the right. Since the two smallest InP segments were out of the measurement range for some of the rotations, the maps include the three largest InP segments and the surrounding GaInP segments only. The upmost maps show the total scattered intensity of the InP and GaInP Bragg peaks in each scanning position. The slightly asymmetric profile of the segments in the maps, with higher intensity above and to the right, comes from a slight asymmetry in the X-ray nanofocusing (Fig. S1(b) in the Electronic Supplementary Material (ESM)). Since the probe profile has tails, no pixel is zero.

The axial strain maps were calculated as the change in lattice constant,  $a$ , compared with the mean value in the map,  $\langle a \rangle$ :  $\epsilon_{\text{axial}} = (a - \langle a \rangle) / \langle a \rangle$ . We used the high intensity pixels in the intensity maps to determine which pixels to show in the strain maps, for clarity. The ones with low total intensity in the scattering signal were set to zero. The average relative difference in lattice constant between the InP and GaInP maps is 1.5%. The total range of measured strain is about 0.14% and 0.42% for the InP and GaInP segments, respectively. We can observe strain variations of less than 0.01%, i.e.  $10^{-4}$ , highlighting the excellent strain sensitivity of XRD.

From the observed mismatch between InP and GaInP and Vegard's law, we calculated the average Ga content in the  $\text{Ga}_x\text{In}_{1-x}\text{P}$  segments to be  $x = 21\%$ , assuming no average strain in the GaInP. In comparison, point measurements from Energy-dispersive X-ray spectroscopy (EDS) of a different nanowire showed a Ga composition of  $x = 36\%$ . From ptychography we obtained a high-resolution map (Fig. S1(a) in the ESM) of the nanowire and note that it is slightly longer, 2.5  $\mu\text{m}$ , compared with the one investigated by STEM, 2.1  $\mu\text{m}$ . This suggests that the nanowire in the XRD maps originated closer to the sample edge, which has a slightly higher growth rate and higher In fraction due to edge effects.

The length of the InP segments has a strong effect on the measured strain, both the average values and the distributions. The InP segments are compressively stressed by the GaInP segments in the radial direction, which intuitively should lead to an expansion in the axial direction that we probe. However, our measurements show a significantly more complex strain distribution. In the two largest InP segments, we indeed observe a lattice expansion (in the axial dimension) towards the surface, but away from the surface the strain is compressive, in particular in the center. In contrast, the 45 nm segment only shows a slight decrease from the center to the surface. The average strain is  $-0.01\%$ ,  $0.00\%$  and  $0.04\%$  in the 170, 80, and 45 nm InP segments, respectively. The observed strain variation within those respective segments is about 0.12%, 0.10% and 0.04%. Note that such small variations would be very challenging to quantify with TEM.

Comparing the GaInP segments with each other, we observe an overall gradient from high to low lattice constant towards the seed particle. This is most likely due to a gradient in the composition of the  $\text{Ga}_x\text{In}_{1-x}\text{P}$  alloy, as previously observed [47, 48]. As a consequence of the growth process, where the In is supplied primarily via surface diffusion, the supply of In decreases the longer the nanowire becomes. Hence, there is a slight gradient in composition such that there is more Ga close to the seed particle than close to the substrate. Therefore, the GaInP lattice and the mismatch to InP become larger along the growth direction, that is, closer to the seed particle. The composition can be calculated from the lattice constant as shown in Fig. S2 in the ESM. We find that the composition changes from  $x = 19\%$  to  $x = 23\%$  between the four segments, implying a gradient of about 3% per  $\mu\text{m}$ . This is in good agreement with measurements of similar nanowires using scanning X-ray fluorescence [47]. Compositional analysis with EDS line scans also shows a sharper change in Ga and In composition when switching from  $\text{Ga}_x\text{In}_{1-x}\text{P}$  to InP than vice versa (Fig. S3 in the ESM).

The strain is also not symmetric within the GaInP segments, where the maximum relative strain is shifted to the left, closer to the seed particle. Thus, within the segments the trend is reversed compared with the overall gradient. An axial asymmetry in strain is also seen in the InP segments, where the strain minima are shifted slightly to the right of the center.



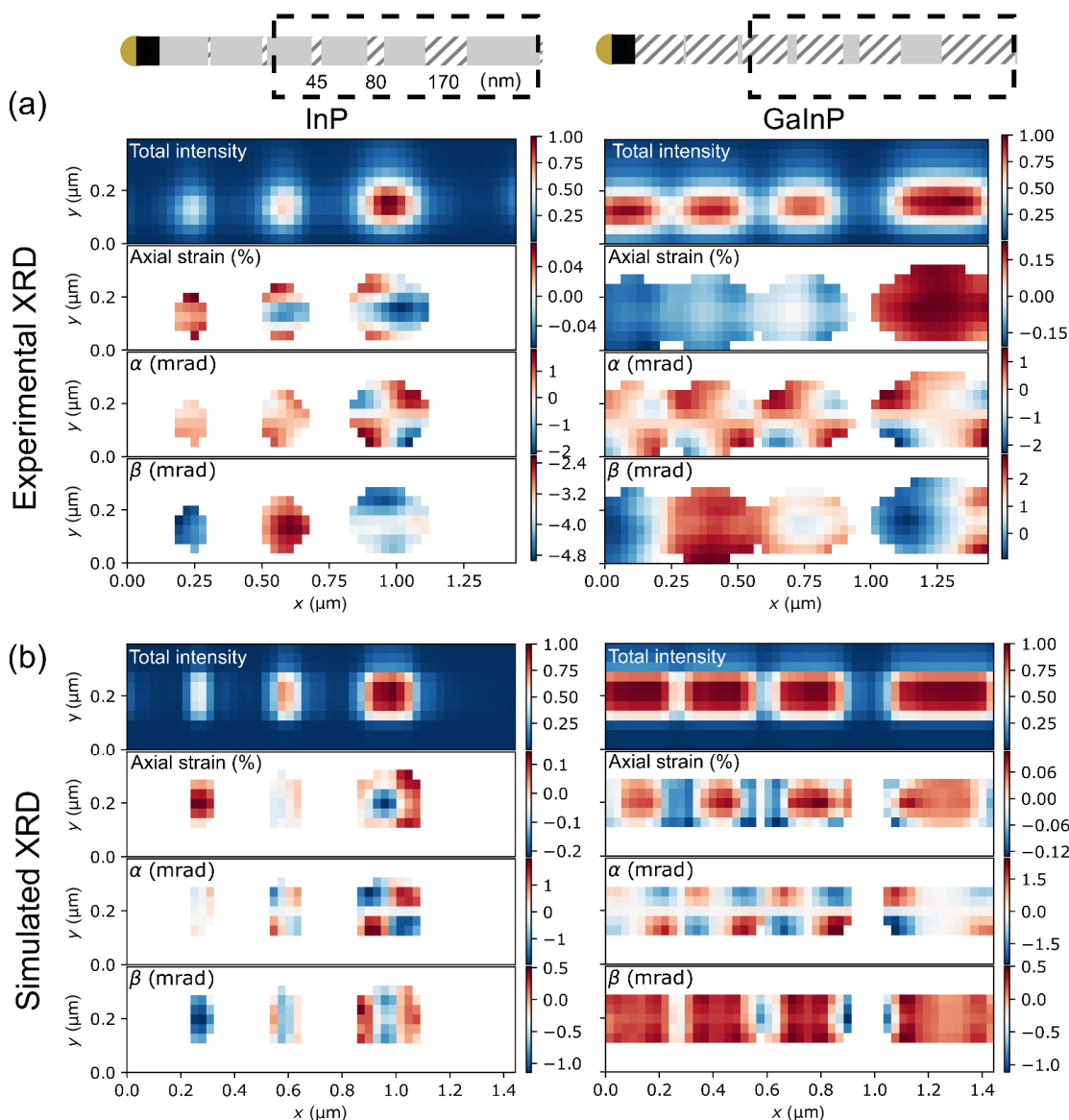


**Figure 2** Scanning XRD experimental results and simulations of a single heterostructured nanowire. The pixel sizes are 30 and 40 nm in the  $x$  and  $y$  directions, respectively. The InP measurements and simulations are shown in the left column, and the GaInP ones in the right column. (a) Experimental results: total scattered intensity in Bragg, axial strain, tilt around  $z$ ,  $\alpha$ , tilt around  $y$ ,  $\beta$ . (b) The corresponding maps from simulated diffraction.

In addition to strain, scanning XRD is very sensitive to small variations in local lattice tilt [28, 49]. From our reciprocal space mapping, we calculate the lattice tilt in two directions: The tilt around  $z$ ,  $\alpha$  and the tilt around  $y$ ,  $\beta$ , see Fig. 1(e). We observe a cross-shaped profile of  $\alpha$  in the largest InP segments, with the strongest tilt at the corners. Following the interface edge or the nanowire surface, the tilt decreases to zero at the center and then changes sign towards the opposite edge. The sensitivity to this tilt is better than 0.1 mrad. A matching tilt distribution is found in the GaInP segments, with the same magnitude but with the sign flipped. Note that we do not find an overall gradient of  $\alpha$ , which would suggest bending of the nanowire in the sample plane.

The distribution of the tilt around  $y$ ,  $\beta$ , is more difficult to analyze. In our measurement geometry, we are very sensitive to tilt around  $z$ ,  $\alpha$ , since it is directly coupled to the vertical position of the Bragg peak on the detector, but we are less sensitive to  $\beta$  as it relies on sampling with the rotation. There seems to be a general gradient in the InP and GaInP segments for the  $\beta$  tilt, changing along the axis from negative to positive back to negative again. Such a gradient is consistent with an

arch shape of the nanowire, possibly due to adhesion to the substrate. The tilt maps could be used to reconstruct the shape of the nanowire in 3D [28], but this is out of the scope of the present work.

### 3.2 FEM simulations of strain

To understand the asymmetries in the strain maps and to confirm the dome shaped strain profiles seen in the tilt maps, we performed a full simulation of the sample and the experiment starting with a 3D FEM strain simulation using the software COMSOL Multiphysics. We used the average measured value for the lattice mismatch, 1.5%, as the initial strain applied to the InP segments (Fig. 3), without any composition gradient or bending of the wire. In Figs. 3(a)–3(d), we show central slices of the 3D simulation, which has radial symmetry, showing the radial (Figs. 3(a) and 3(c)) and axial (Figs. 3(b) and 3(d)) strain components. The axial component is the one that is measured in our experiment. Near the segment interfaces, the InP crystal, which has the larger lattice constant, is radially compressively strained (shown in blue) while the GaInP is tensile strained (shown in red), see Fig. 3(a). The strain distributions

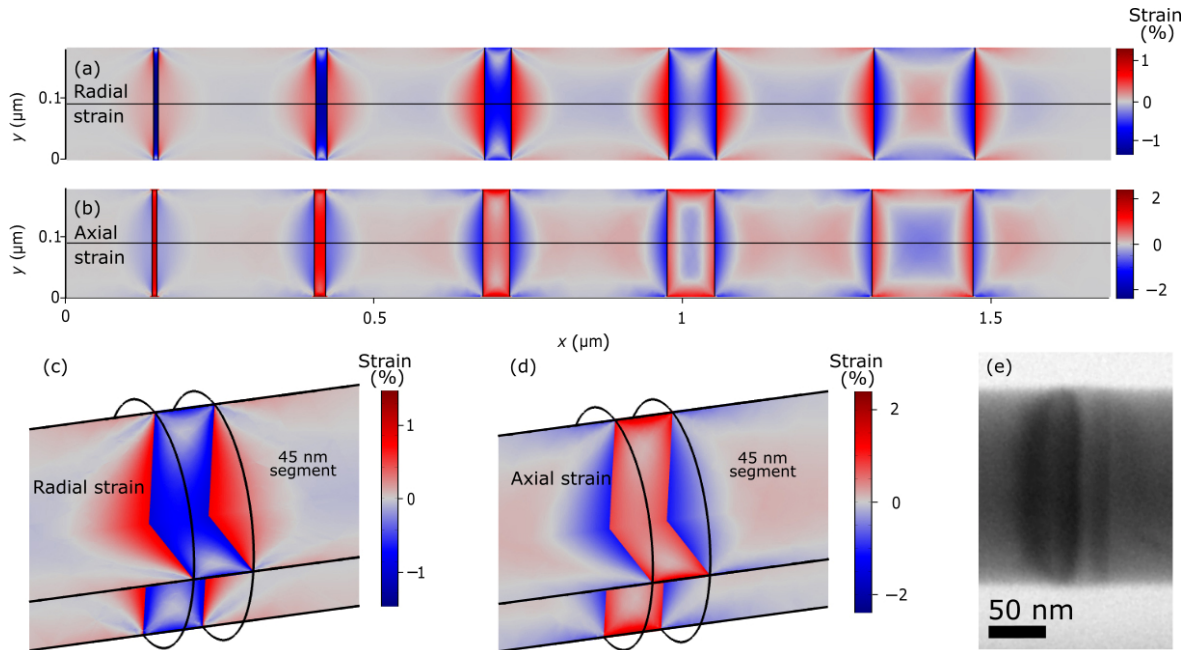


**Figure 3** (a)–(d) 3D FEM simulations of elastic strain caused by a lattice mismatch of 1.5% between the segments. (a) Strain along the radial dimension in a central slice of the nanowire. (b) Strain in the axial dimension of the nanowire. (c) Strain in the radial dimension; a two-cut plot of the 45 nm segment. (d) Strain in the axial dimension of the nanowire; a two-cut plot of the 45 nm segment. All the strain results are radially symmetric. (e) STEM aligned in a  $\langle 112 \rangle$  direction of a 45 nm segment.

form dome shapes at the segment interfaces, qualitatively in line with previous simulations [25, 27]. As expected, the crystal expands in the axial direction where it compresses radially, as shown in Fig. 3(b). The magnitude of the strain is about twice as large in the axial dimension, again in agreement with previously reported simulations [27].

A closer view of the 45 nm segment is seen in Figs. 3(c) and 3(d). As a comparison, we show STEM of a 45 nm segment in a nanowire from the same sample in Fig. 3(e). The strain gives rise to contrast due to a Moiré effect, showing a dome shaped profile in excellent qualitative agreement with our FEM simulations. Quantifying the strain from such a STEM image is challenging, however. The STEM also shows that the InP segment has a slightly larger radius, about 2–4 nm more than the surrounding GaInP segments, something that is not resolved in the XRD strain maps. The FEM simulations predict that the lateral strain relaxation leads to a maximum radial displacement of 1.3 nm. Note that there could be a slight radial growth on the InP segment as well, despite the use of *in situ* HCl etching during growth [50], which is not included in the simulations.

### 3.3 Simulated scanning XRD

The FEM simulations generate the 3D strain and the displacement field,  $u(\mathbf{r})$ , where  $\mathbf{r}$  is the real space coordinate, with very high real-space resolution. The axial strain component cannot be directly compared with the experimental strain maps, since in the measurement the axial strain is convoluted with the footprint of the beam. The beam creates an averaging effect that is complicated by the complex profile. Therefore, we made a full simulation of the scanning XRD experiment. For each beam position  $j$ , we calculated the exit wave  $\Psi_j$  using the Bragg vector  $\mathbf{G}_{\text{hkl}}$  ( $|\mathbf{G}_{111}| = 1.85 \text{ \AA}^{-1}$  for InP and  $|\mathbf{G}_{111}| = 1.92 \text{ \AA}^{-1}$  for  $\text{Ga}_x\text{In}_{1-x}\text{P}$  with  $x = 21\%$ ) and the probe function  $P(\mathbf{r})$  as [51, 52]

$$\Psi_j = |\rho_j(\mathbf{r})| e^{i\mathbf{G}_{\text{hkl}} \cdot \mathbf{u}_j(\mathbf{r})} P(\mathbf{r})$$

The electron density in a single position,  $\rho_j(\mathbf{r})$  was represented

as a binary shape function. The probe profile at focus,  $P(\mathbf{r})$ , was reconstructed from a ptychographic measurement on a Siemens star test sample (Fig. S1(b) in the ESM). Next, the exit wave was propagated to the far field with a Fourier transform, and the intensity on the Bragg detector in one probe position was calculated as  $I_j = |\mathcal{F}(\Psi_j)|^2$ .

We show a comparison of an experimental and a simulated Bragg peak in Fig. 4, with the three central cuts when the beam is centered on the 170 nm InP segment. Qualitatively, the simulated Bragg peaks show many similarities with the measured ones. The shape of the Bragg peak is largely determined by the Fourier transform of the shape function of the segment. The cuts perpendicular to  $q_x$  and  $q_y$  (left and right), show the Fourier transform of the square dimensions of the segment, but the strain gradients curve the shape of the fringes. Correspondingly, the cut perpendicular to  $q_z$  (middle) shows the Fourier transform of the circular dimension. To better illustrate the appearance of the 3D Bragg peak and how it is affected by strain, we also show an idealized simulation with a high-flux plane wave probe and smaller pixels in Fig. S4 in the ESM.

The final step in the simulation is to make a center of mass analysis of the Bragg peaks at each position, just like the measured data is treated. The simulated intensity, strain and tilt maps are shown together with the measured ones in Fig. 2(b). Overall, we find excellent qualitative agreement between the simulated and measured strain and tilt maps. In the following, we will discuss similarities and differences between the simulations and measurements in detail.

### 3.4 Discussion

In the large InP and GaInP segments, both the simulation and the measurements show that the strain in the central parts of the segments changes sign compared with the edges. For instance, the largest InP segment shows an intuitively expected tensile radial strain near the mismatched heterointerfaces, but also a slight compressive strain in the center. With decreasing

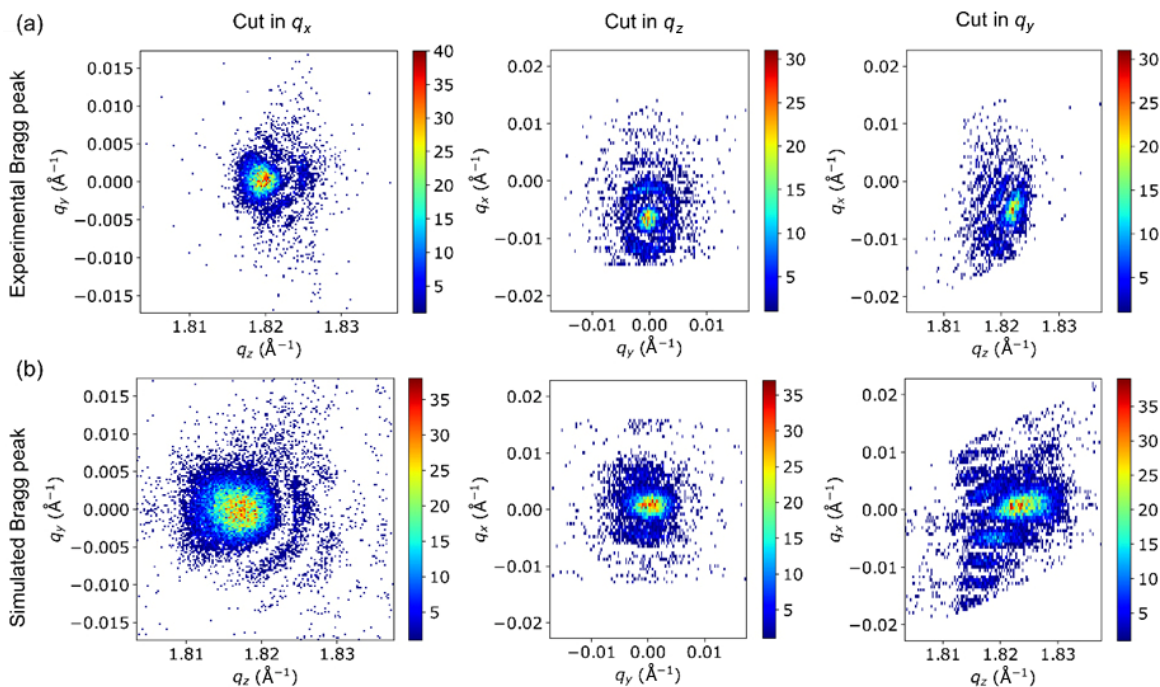


**Figure 4** Three central cuts of diffraction from the 170 nm InP segment presented in an orthogonal system. (a) Measured scattering with an acquisition time of 0.12 s for each frame. (b) Simulated scattering calculated from the displacement field from the FEM model (Fig. 3(b)) and the experimental probe as reconstructed from ptychography (Fig. S1(b) in the ESM).

segment length, the strain in the InP segments increases, and for the two shortest InP segments, almost the entire segments have the same lattice constant as GaInP. Comparing the InP segments with each other, the trend is that in the radial direction the lattice in the shorter segments adapts more to the surrounding GaInP crystal.

Comparing the GaInP segments with the largest InP segment, we find a similar but inverted strain distribution in both the simulations and the measurements. Since the GaInP simulations did not include the axial gradient in the Ga composition, the strain profiles in the different segments are similar to each other.

The simulated lattice tilt,  $\alpha$ , shows excellent quantitative and qualitative agreement with the measurements. Evidently, the sign shift comes from the dome-shaped strain profile, which means that the crystal is tilted in the opposite direction in each half across the nanowire. This can be seen in the measured and simulated XRD in Fig. 2(a) and 2(b), respectively. The tilt is not affected by the  $\text{Ga}_x\text{In}_{1-x}\text{P}$  composition gradient. The tilt around  $y$ ,  $\beta$ , in the measurements is dominated by an overall arch shaped bending of the nanowire, which is not included in the simulations.

While the simulations are qualitatively similar to the measurements, the quantitative comparison is less consistent. The simulated strain in the InP segments is about twice as large in the simulations as in the measurement. This could indicate that dislocations, which are not included in the FEM simulations, may have formed in the measured nanowire as a result of the lattice mismatch, since dislocations would reduce the strain. However, the tilt around  $z$ ,  $\alpha$ , is only marginally smaller in the measurements, which should not be possible with a partially relaxed strain. Instead, the difference in absolute strain could be due to limitations in the spatial resolution. The convolution of the 90 nm probe and the FEM modeled nanowire creates an average that serves to reduce the extreme values in the FEM model quite significantly. The intensity maps in the simulated XRD show segment edges with sharper profiles than

in the measurements, which, together with the observation that the central structures in the simulated diffraction patterns are slightly larger than the measured ones, indicates the probe was slightly larger than anticipated in the experiment. A larger probe would increase the averaging effect and hence reduce the strain range. Possibly, the nanowire was slightly out of focus. The most extreme strain values could be further blurred by imperfections in beam intensity and the scanning and rotation motors. Note that the measurement of the  $\alpha$  tilt, which shows a much better agreement, relies only on the vertical center of mass on the detector, and is independent of the rotation motor and intensity fluctuations. In this sense,  $\alpha$  in scanning XRD is similar to differential phase contrast in scanning transmission X-ray microscopy (STXM) [53].

## 4 Conclusions

To conclude, we have demonstrated high-resolution strain mapping of an axial nanowire heterostructured using scanning X-ray diffraction. This was performed at the first DLSR, MAX IV, where we obtained 2D strain maps with about  $10^{-4}$  relative strain resolution. Several assumptions were made for the FEM model, such as perfectly sharp heterojunctions, no strain accommodation via defects, and no bending. High-resolution strain measurements were necessary to test these assumptions, which have previously been used in theoretical reports. The strain maps and the complementing simulations show how the strain relaxes at the surface of the nanowire, as previously theoretically predicted. We find that the InP segment length has profound quantitative and qualitative effects on the strain distribution. The largest segments show a complex 3D variation with both compressive and tensile strain, differing strongly from thin film growth, while the shortest measured InP segment is almost fully adapted to the GaInP lattice. The different strain profiles can have a strong effect on the electronic and optical properties of the InP segments. The positively (tensile) strained regions should have a reduced local band gap, which for instance



leads to a localization of optically excited charge carriers. In the two longest InP segments, the most positively axially strained region is found in the center, while in the 40 nm segment this region forms a ring around the center. Our diffraction simulations show how the averaging of the probe changes the quantification of strain from a FEM model, highlighting the importance of simulating the experiment with a realistic model of the X-ray focus to be able to compare with measurements. The results demonstrate that nano-XRD can reach sufficient spatial resolution to quantitatively map the strain field in heterostructured nanowires.

Further improvements in spatial resolution should also lead to enhanced sensitivity to spatial variations in strain. The most straightforward strategy to improve the spatial resolution is to develop the X-ray optics, where the state of the art currently reaches around and slightly below 10 nm [33, 54]. An alternative approach is to take advantage of the coherence of the X-rays and use phase retrieval methods [51, 55, 56] to achieve sub-beam spatial resolution. The present study was one of the first at the NanoMAX beamline, which can currently deliver about 10 times more coherent flux than at the time of the present experiment [57], making it an ideal system for coherent Bragg methods.

## 5 Methods

### 5.1 Growth

The Au seed particle array was defined on a 2" InP (111)B wafer by nanoimprint lithography, reactive ion etching, metal evaporation, and lift-off, resulting in a hexagonal pattern of Au particles with a pitch of 500 nm [44]. The imprinted InP wafer was cleaved into smaller samples used for growth.

The nanowires were grown in a low pressure (100 mbar) metal-organic vapor phase epitaxy system (Aixtron 200/4) with a total flow of 13 L/min and H<sub>2</sub> as the carrier gas. In order to improve pattern preservation, a pre-anneal nucleation step [44] was performed at 280 °C for 1 min with molar fractions of trimethylindium (TMIn) of  $\chi_{\text{TMIn}} = 8.9 \times 10^{-5}$  and phosphine (PH<sub>3</sub>) of  $\chi_{\text{PH}_3} = 6.9 \times 10^{-3}$ . Then the sample was annealed for 10 min at 550 °C under  $\chi_{\text{PH}_3} = 3.5 \times 10^{-2}$  to desorb surface oxides. After annealing, the chamber was cooled to 440 °C. The growth was initiated with an InP nucleation step by adjusting PH<sub>3</sub> to  $\chi_{\text{PH}_3} = 6.9 \times 10^{-3}$  and introducing TMIn with  $\chi_{\text{TMIn}} = 8.9 \times 10^{-5}$ . After 15 s, HCl was introduced at a molar fraction of  $\chi_{\text{HCl}} = 4.6 \times 10^{-5}$  to eliminate radial growth [50, 58]. After a total of 60 s InP growth, 4 min of InGaP growth was carried out by introducing trimethylgallium (TMGa) at a molar fraction of  $\chi_{\text{TMGa}} = 1.4 \times 10^{-3}$  and by switching the other precursors to  $\chi_{\text{TMIn}} = 2.7 \times 10^{-5}$ ,  $\chi_{\text{PH}_3} = 5.4 \times 10^{-3}$ , and  $\chi_{\text{HCl}} = 5.4 \times 10^{-5}$ . After this, a barcode sequence was grown by alternating between InP,  $\chi_{\text{TMIn}} = 5.4 \times 10^{-5}$ , and InGaP,  $\chi_{\text{TMIn}} = 2.7 \times 10^{-5}$  and  $\chi_{\text{TMGa}} = 1.4 \times 10^{-3}$ . PH<sub>3</sub> and HCl were kept constant as in the previous step. The 10 segments were grown each for 2 min, 2 min 50 s, 1 min, 3 min, 45 s, 3 min 10 s, 30 s, 3 min 20 s, 15 s, and 3 min 41 s, respectively. After the barcode sequence, TMIn was switched off for 2 min, while keeping PH<sub>3</sub>, HCl, and TMGa unchanged. Finally, the flows of TMGa and HCl were switched off and the chamber was cooled to 300 °C under a PH<sub>3</sub>/H<sub>2</sub> gas mixture.

### 5.2 TEM

For TEM measurements a JEOL 3000F was used. The nanowires were transferred to a lacey carbon copper grid by gently rubbing it on the growth substrate.

### 5.3 Nano-XRD

The nanowire sample holder was mounted in the nanofocus on top of a piezoelectric scanning stage. The Si<sub>3</sub>N<sub>4</sub> window was located with transmission and X-ray fluorescence signal, which also showed contrast for single nanowires. Single nanowires were aligned horizontally using ptychography in the forward direction.

In transmission, we used a Pilatus 100K detector with 172 μm pixel size placed 4.2 m downstream of the nanofocus. Simultaneously, a Merlin detector with pixel size 55 μm was used in Bragg geometry 1.15 m from the nanofocus. Furthermore, the fluorescence signal was collected with an Amptek silicon drift detector close to the sample.

The transmission signal was used to track real space movements during the experiment, with STXM and ptychography. In a rocking curve, we saw systematic and unsystematic movements of the sample (see Fig. S5 in the ESM). To correct for these movements, we used maps of the summed Bragg intensity. We defined a small regular grid and connected each Bragg diffraction image to the correct position in real space (see Fig. S6 in the ESM for comparison).

The 3D Bragg peaks were sampled in the skewed reciprocal coordinate system ( $q_1, q_2, q_3$ ), so the data was first converted to a Cartesian coordinate system to facilitate analysis. Then, the two centers of mass of the Bragg peaks were calculated for each scan point, giving their positions in reciprocal space. From these positions, we calculated the length of the scattering vector  $Q$  and the resulting local lattice constant,  $a$ , as well as the two lattice tilts.

The absolute values of the lattice constants were estimated from a calibration of the  $2\theta$  angle (the position of the Bragg detector) in the setup. By comparing the measured  $a_{\text{InP}}$  to the literature value  $a_{\text{InP}} = 5.8687 \text{ \AA}$ , we corrected  $a_{\text{GaInP}}$  with the same systematic error.

The beam profile was found from ptychographic reconstructions in the forward direction, on a Siemens star test sample, at the beginning and end of the beamtime (Fig. S1(b) in the ESM).

We observed no decay in the scattered signal over the measurement time, indicating insignificant beam damage to the wires.

### 5.4 Simulations

FEM simulation were performed using an isotropic linear elasticity model in the simulation software COMSOL Multiphysics. We used bulk literature values for the material parameters. For Ga<sub>x</sub>In<sub>1-x</sub>P, we used interpolated values, assuming  $x = 21\%$ . The nanowire stub of InP of 10 nm was included in the COMSOL model but not shown in the figures. The end of the stub was constrained to be fixed in the simulation. The 2D probe profile was reconstructed from ptychography and normalized to a total intensity of 10<sup>9</sup> to match the experimental flux, then propagated to 3D. Then we applied a Poisson noise to the intensity with the rate parameter ( $\lambda = 2$  to 25) adjusted to match the measured data.

## Acknowledgements

We acknowledge the excellent support from the staff at the MAX IV Laboratory, in particular Gerardina Carbone for the preparations at the NanoMAX beamline. The MAX IV Laboratory receives funding through the Swedish Research Council under grant no 2013-02235. This research was funded by the Röntgen-Ångström Cluster, NanoLund, Marie Skłodowska Curie Actions, Cofund, Project INCA 600398, and the Swedish

Research Council grant number 2015-00331. L. J. L. and M. O. H. acknowledge support of NSF DMR 1611341 and 1905768. M. O. H. acknowledges support of the NSF GRFP and the NSF GROW program.

**Funding note:** Open access funding provided by Lund University.

**Electronic Supplementary Material:** Supplementary material (scanning XRD analysis details, compositional analysis with EDS, simulation and experimental details) is available in the online version of this article at <https://doi.org/10.1007/s12274-020-2878-6>.

**Open Access** This article is licensed under a Creative Commons Attribution 4.0 International License, which permits use, sharing, adaptation, distribution and reproduction in any medium or format, as long as you give appropriate credit to the original author(s) and the source, provide a link to the Creative Commons licence, and indicate if changes were made.

The images or other third party material in this article are included in the article's Creative Commons licence, unless indicated otherwise in a credit line to the material. If material is not included in the article's Creative Commons licence and your intended use is not permitted by statutory regulation or exceeds the permitted use, you will need to obtain permission directly from the copyright holder.

To view a copy of this licence, visit <http://creativecommons.org/licenses/by/4.0/>.

## References

- Memisevic, E.; Hellenbrand, M.; Lind, E.; Persson, A. R.; Sant, S.; Schenk, A.; Svensson, J.; Wallenberg, R.; Wernersson, L. E. Individual defects in InAs/InGaAsSb/GaSb nanowire tunnel field-effect transistors operating below 60 mV/decade. *Nano Lett.* **2017**, *17*, 4373–4380.
- Tomioka, K.; Yoshimura, M.; Fukui, T. A III–V nanowire channel on silicon for high-performance vertical transistors. *Nature* **2012**, *488*, 189–192.
- Jia, C. C.; Lin, Z. Y.; Huang, Y.; Duan, X. F. Nanowire electronics: From nanoscale to macroscale. *Chem. Rev.* **2019**, *119*, 9074–9135.
- Haverkort, J. E. M.; Garnett, E. C.; Bakkers, E. P. A. M. Fundamentals of the nanowire solar cell: Optimization of the open circuit voltage. *Appl. Phys. Rev.* **2018**, *5*, 031106.
- Otnes, G.; Borgström, M. T. Towards high efficiency nanowire solar cells. *Nano Today* **2017**, *12*, 31–45.
- Wallentin, J.; Anttu, N.; Asoli, D.; Huffman, M.; Åberg, I.; Magnusson, M. H.; Siefer, G.; Fuss-Kailuweit, P.; Dimroth, F.; Witzigmann, B. et al. InP nanowire array solar cells achieving 13.8% efficiency by exceeding the ray optics limit. *Science* **2013**, *339*, 1057–1060.
- Soci, C.; Zhang, A.; Bao, X. Y.; Kim, H.; Lo, Y.; Wang, D. L. Nanowire photodetectors. *J. Nanosci. Nanotechnol.* **2010**, *10*, 1430–1449.
- Gudiksen, M. S.; Lauhon, L. J.; Wang, J. F.; Smith, D. C.; Lieber, C. M. Growth of nanowire superlattice structures for nanoscale photonics and electronics. *Nature* **2002**, *415*, 617–620.
- Gibson, S. J.; van Kasteren, B.; Tekcan, B.; Cui, Y. C.; van Dam, D.; Haverkort, J. E.; Bakkers, E. P. A. M.; Reimer, M. E. Tapered InP nanowire arrays for efficient broadband high-speed single-photon detection. *Nat. Nanotechnol.* **2019**, *14*, 473–479.
- Barrigón, E.; Heurlin, M.; Bi, Z. X.; Monemar, B.; Samuelson, L. Synthesis and applications of III–V nanowires. *Chem. Rev.* **2019**, *119*, 9170–9220.
- Motohisa, J.; Kameda, H.; Sasaki, M.; Tomioka, K. Characterization of nanowire light-emitting diodes grown by selective-area metal-organic vapor-phase epitaxy. *Nanotechnology* **2019**, *30*, 134002.
- Corfdir, P.; Marquardt, O.; Lewis, R. B.; Sinito, C.; Ramsteiner, M.; Trampert, A.; Jahn, U.; Geelhaar, L.; Brandt, O.; Fomin, V. M. Excitonic Aharonov–Bohm oscillations in core–shell nanowires. *Adv. Mater.* **2019**, *31*, 1805645.
- Mourik, V.; Zuo, K.; Frolov, S. M.; Plissard, S.; Bakkers, E. P. A. M.; Kouwenhoven, L. P. Signatures of Majorana fermions in hybrid superconductor–semiconductor nanowire devices. *Science* **2012**, *336*, 1003–1007.
- Zhang, H.; Liu, D. E.; Wimmer, M.; Kouwenhoven, L. P. Next steps of quantum transport in Majorana nanowire devices. *Nat. Commun.* **2019**, *10*, 5128.
- Świdorski, M.; Zieliński, M. Electric field tuning of excitonic fine-structure splitting in asymmetric InAs/InP nanowire quantum dot molecules. *Phys. Rev. B* **2019**, *100*, 235417.
- Haffouz, S.; Zeuner, K. D.; Dalacu, D.; Poole, P. J.; Lapointe, J.; Poitras, D.; Mnaymneh, K.; Wu, X. H.; Couillard, M.; Korkusinski, M. et al. Bright single InAsP quantum dots at telecom wavelengths in position-controlled InP nanowires: The role of the photonic waveguide. *Nano Lett.* **2018**, *18*, 3047–3052.
- Björk, M. T.; Ohlsson, B. J.; Sass, T.; Persson, A. I.; Thelander, C.; Magnusson, M. H.; Deppert, K.; Wallenberg, L. R.; Samuelson, L. One-dimensional heterostructures in semiconductor nanowhiskers. *Appl. Phys. Lett.* **2002**, *80*, 1058–1060.
- Lauhon, L. J.; Gudiksen, M. S.; Wang, D. L.; Lieber, C. M. Epitaxial core–shell and core–multishell nanowire heterostructures. *Nature* **2002**, *420*, 57–61.
- Josefsson, M.; Svilans, A.; Burke, A. M.; Hoffmann, E. A.; Fahlvik, S.; Thelander, C.; Leijnse, M.; Linke, H. A quantum-dot heat engine operating close to the thermodynamic efficiency limits. *Nat. Nanotechnol.* **2018**, *13*, 920–924.
- LaPierre, R. R.; Chia, A. C. E.; Gibson, S. J.; Haapamaki, C. M.; Boulanger, J.; Yee, R.; Kuyanov, P.; Zhang, J.; Tajik, N.; Jewell, N. et al. III–V nanowire photovoltaics: Review of design for high efficiency. *Phys. Status Solidi* **2013**, *7*, 815–830.
- Yao, M. Q.; Cong, S.; Arab, S.; Huang, N. F.; Povinelli, M. L.; Cronin, S. B.; Dapkus, P. D.; Zhou, C. W. Tandem solar cells using GaAs nanowires on Si: Design, fabrication, and observation of voltage addition. *Nano Lett.* **2015**, *15*, 7217–7224.
- Zeng, X. L.; Otnes, G.; Heurlin, M.; Mourão, R. T.; Borgström, M. T. InP/GaInP nanowire tunnel diodes. *Nano Res.* **2018**, *11*, 2523–2531.
- Saxena, D.; Mokkapatil, S.; Parkinson, P.; Jiang, N.; Gao, Q.; Tan, H. H.; Jagadish, C. Optically pumped room-temperature GaAs nanowire lasers. *Nat. Photonics* **2013**, *7*, 963–968.
- Ertekin, E.; Greaney, P. A.; Chrzan, D. C.; Sands, T. D. Equilibrium limits of coherency in strained nanowire heterostructures. *J. Appl. Phys.* **2005**, *97*, 114325.
- Ye, H.; Lu, P. F.; Yu, Z. Y.; Song, Y. X.; Wang, D. L.; Wang, S. M. Critical thickness and radius for axial heterostructure nanowires using finite-element method. *Nano Lett.* **2009**, *9*, 1921–1925.
- Glas, F. Critical dimensions for the plastic relaxation of strained axial heterostructures in free-standing nanowires. *Phys. Rev. B* **2006**, *74*, 121302.
- Glas, F. Strain in nanowires and nanowire heterostructures. *Semicond. Semimet.* **2015**, *93*, 79–123.
- Wallentin, J.; Jacobsson, D.; Osterhoff, M.; Borgstrom, M. T.; Salditt, T. Bending and twisting lattice tilt in strained core-shell nanowires revealed by nanofocused X-ray diffraction. *Nano Lett.* **2017**, *17*, 4143–4150.
- Sköld, N.; Wagner, J. B.; Karlsson, G.; Hernán, T.; Seifert, W.; Pistol, M. E.; Samuelson, L. Phase segregation in AlInP shells on GaAs nanowires. *Nano Lett.* **2006**, *6*, 2743–2747.
- Wen, C. Y.; Reuter, M. C.; Su, D.; Stach, E. A.; Ross, F. M. Strain and stability of ultrathin Ge layers in Si/Ge/Si axial heterojunction nanowires. *Nano Lett.* **2015**, *15*, 1654–1659.
- Larsson, M. W.; Wagner, J. B.; Wallin, M.; Håkansson, P.; Fröberg, L. E.; Samuelson, L.; Reine Wallenberg, L. Strain mapping in free-standing heterostructured wurtzite InAs/InP nanowires. *Nanotechnology* **2007**, *18*, 015504.
- Schropp, A.; Hoppe, R.; Patommel, J.; Samberg, D.; Seiboth, F.; Stephan, S.; Wellenreuther, G.; Falkenberg, G.; Schroer, C. G. Hard X-ray scanning microscopy with coherent radiation: Beyond the resolution of conventional X-ray microscopes. *Appl. Phys. Lett.* **2012**, *100*, 253112.



- [33] Döring, F.; Robisch, A. L.; Eberl, C.; Osterhoff, M.; Ruhlandt, A.; Liese, T.; Schlenkrich, F.; Hoffmann, S.; Bartels, M.; Salditt, T. et al. Sub-5 nm hard X-ray point focusing by a combined Kirkpatrick-Baez mirror and multilayer zone plate. *Opt. Express* **2013**, *21*, 19311–19323.
- [34] Schülly, T. U.; Leake, S. J. X-ray nanobeam diffraction imaging of materials. *Curr. Opin. Solid State Mater. Sci.* **2018**, *22*, 188–201.
- [35] Stankevič, T.; Hilner, E.; Seiboth, F.; Ciecchonski, R.; Vescovi, G.; Kryliouk, O.; Johansson, U.; Samuelson, L.; Wellenreuther, G.; Falkenberg, G. et al. Fast strain mapping of nanowire light-emitting diodes using nanofocused X-ray beams. *ACS Nano* **2015**, *9*, 6978–6984.
- [36] Biermanns, A.; Breuer, S.; Davydok, A.; Geelhaar, L.; Pietsch, U. Structural polytypism and residual strain in GaAs nanowires grown on Si(111) probed by single-nanowire X-ray diffraction. *J. Appl. Cryst.* **2012**, *45*, 239–244.
- [37] Keplinger, M.; Mandl, B.; Kriegner, D.; Holý, V.; Samuelsson, L.; Bauer, G.; Deppert, K.; Stangl, J. X-ray diffraction strain analysis of a single axial InAs<sub>1-x</sub>P<sub>x</sub> nanowire segment. *J. Synchrotron Radiat.* **2015**, *22*, 59–66.
- [38] Jacques, V. L. R.; Carbone, D.; Ghisleni, R.; Thilly, L. Counting dislocations in microcrystals by coherent X-ray diffraction. *Phys. Rev. Lett.* **2013**, *111*, 065503.
- [39] Hrauda, N.; Zhang, J. J.; Wintersberger, E.; Eitzelstorfer, T.; Mandl, B.; Stangl, J.; Carbone, D.; Holý, V.; Jovanović, V.; Biasotto, C. et al. X-ray nanodiffraction on a single size quantum dot inside a functioning field-effect transistor. *Nano Lett.* **2011**, *11*, 2875–2880.
- [40] Lazarev, S.; Dzhigaev, D.; Bi, Z. X.; Nowzari, A.; Kim, Y. Y.; Rose, M.; Zaluzhnyy, I. A.; Gorobtsov, O. Y.; Zozulya, A. V.; Lenrick, F. et al. Structural changes in a single GaN nanowire under applied voltage bias. *Nano Lett.* **2018**, *18*, 5446–5452.
- [41] Wallentin, J.; Osterhoff, M.; Salditt, T. In operando X-ray nanodiffraction reveals electrically induced bending and lattice contraction in a single nanowire device. *Adv. Mater.* **2016**, *28*, 1788–1792.
- [42] Eriksson, M.; van der Veen, J. F.; Quitmann, C. Diffraction-limited storage rings—A window to the science of tomorrow. *J. Synchrotron Radiat.* **2014**, *21*, 837–842.
- [43] Vogt, U.; Parfeniukas, K.; Stankevič, T.; Kalbfleisch, S.; Liebi, M.; Matej, Z.; Björling, A.; Carbone, G.; Mikkelsen, A.; Johansson, U. First X-ray nanoimaging experiments at nanomax. In *Proceedings of X-Ray Nanoimaging: Instruments and Methods III 2017*, San Diego, USA, 2017; p 7.
- [44] Otnes, G.; Heurlin, M.; Graczyk, M.; Wallentin, J.; Jacobsson, D.; Berg, A.; Maximov, I.; Borgström, M. T. Strategies to obtain pattern fidelity in nanowire growth from large-area surfaces patterned using nanoimprint lithography. *Nano Res.* **2016**, *9*, 2852–2861.
- [45] Björling, A.; Kalbfleisch, S.; Kahnt, M.; Sala, S.; Parfeniukas, K.; Vogt, U.; Carbone, D.; Johansson, U. Ptychographic characterization of a coherent nanofocused X-ray beam. *Opt. Express* **2020**, *28*, 5069–5076.
- [46] Chahine, G. A.; Richard, M. I.; Homs-Regojo, R. A.; Tran-Caliste, T. N.; Carbone, D.; Jaques, V. L. R.; Grifone, R.; Boesecke, P.; Katzer, J.; Costina, I. et al. Imaging of strain and lattice orientation by quick scanning X-ray microscopy combined with three-dimensional reciprocal space mapping. *J. Appl. Cryst.* **2014**, *47*, 762–769.
- [47] Troian, A.; Otnes, G.; Zeng, X. L.; Chayanun, L.; Dagytė, V.; Hammarberg, S.; Salomon, D.; Timm, R.; Mikkelsen, A.; Borgström, M. T. et al. Nanobeam X-ray fluorescence dopant mapping reveals dynamics of *in situ* Zn-doping in nanowires. *Nano Lett.* **2018**, *18*, 6461–6468.
- [48] Otnes, G.; Heurlin, M.; Zeng, X. L.; Borgström, M. T. In<sub>x</sub>Ga<sub>1-x</sub>P nanowire growth dynamics strongly affected by doping using diethylzinc. *Nano Lett.* **2017**, *17*, 702–707.
- [49] Eitzelstorfer, T.; Süess, M. J.; Schiefler, G. L.; Jacques, V. L. R.; Carbone, D.; Chrastina, D.; Isella, G.; Spolenak, R.; Stangl, J.; Sigg, H. et al. Scanning X-ray strain microscopy of inhomogeneously strained Ge micro-bridges. *J. Synchrotron Radiat.* **2014**, *21*, 111–118.
- [50] Borgström, M. T.; Wallentin, J.; Trägårdh, J.; Ramvall, P.; Ek, M.; Wallenberg, L. R.; Samuelson, L.; Deppert, K. *In situ* etching for total control over axial and radial nanowire growth. *Nano Res.* **2010**, *3*, 264–270.
- [51] Godard, P.; Carbone, G.; Allain, M.; Mastrogiuseppe, F.; Chen, G.; Capello, L.; Diaz, A.; Metzger, T. H.; Stangl, J.; Chamard, V. Three-dimensional high-resolution quantitative microscopy of extended crystals. *Nat. Commun.* **2011**, *2*, 568.
- [52] Robinson, I.; Harder, R. Coherent X-ray diffraction imaging of strain at the nanoscale. *Nat. Mater.* **2009**, *8*, 291–298.
- [53] Bunk, O.; Bech, M.; Jensen, T. H.; Feidenhans'l, R.; Binderup, T.; Menzel, A.; Pfeiffer, F. Multimodal X-ray scatter imaging. *New J. Phys.* **2009**, *11*, 123016.
- [54] Bajt, S.; Prasciolu, M.; Fleckenstein, H.; Domaracký, M.; Chapman, H. N.; Morgan, A. J.; Yefanov, O.; Messerschmidt, M.; Du, Y.; Murray, K. T. et al. X-ray focusing with efficient high-NA multilayer laue lenses. *Light Sci. Appl.* **2018**, *7*, 17162.
- [55] Hill, M. O.; Calvo-Almazan, I.; Allain, M.; Holt, M. V.; Ulvestad, A.; Treu, J.; Koblmüller, G.; Huang, C. Y.; Huang, X. J.; Yan, H. F. et al. Measuring three-dimensional strain and structural defects in a single InGaAs nanowire using coherent X-ray multiangle Bragg projection ptychography. *Nano Lett.* **2018**, *18*, 811–819.
- [56] Pfeifer, M. A.; Williams, G. J.; Vartanyants, I. A.; Harder, R.; Robinson, I. K. Three-dimensional mapping of a deformation field inside a nanocrystal. *Nature* **2006**, *442*, 63–66.
- [57] Björling, A.; Carbone, D.; Sarabia, F. J.; Hammarberg, S.; Feliu, J. M.; Solla-Gullón, J. Coherent Bragg imaging of 60 nm Au nanoparticles under electrochemical control at the nanomax beamline. *J. Synchrotron Radiat.* **2019**, *26*, 1830–1834.
- [58] Jacobsson, D.; Persson, J. M.; Kriegner, D.; Eitzelstorfer, T.; Wallentin, J.; Wagner, J. B.; Stangl, J.; Samuelson, L.; Deppert, K.; Borgström, M. T. Particle-assisted Ga<sub>x</sub>In<sub>1-x</sub>P nanowire growth for designed bandgap structures. *Nanotechnology* **2012**, *23*, 245601.